

# Supporting Information for Ephemerality of discrete methane vents in lake sediments

Benjamin P. Scandella<sup>1</sup>, Liam Pillsbury<sup>2</sup>, Thomas Weber<sup>2</sup>,  
Carolyn Ruppel<sup>3</sup>, Harold F. Hemond<sup>1</sup>, Ruben Juanes<sup>1,\*</sup>

<sup>1</sup> Department of Civil and Environmental Engineering, Massachusetts Institute of Technology

<sup>2</sup> Department of Mechanical Engineering, University of New Hampshire

<sup>3</sup> US Geological Survey, Woods Hole, Massachusetts, USA.

\*E-mail: juanes@mit.edu

## Contents

<b>1</b>	<b>Deployment locations</b>	<b>2</b>
<b>2</b>	<b>Flux estimation methods</b>	<b>2</b>
2.1	Backscatter measurement using the Imagenex 837B . . . . .	2
2.2	Backscatter vs. flux for a multibeam sonar . . . . .	3
2.3	Calibration experiment . . . . .	7
2.4	Classification of events . . . . .	9
2.5	Beam pattern . . . . .	9
<b>3</b>	<b>Analysis of flux magnitudes</b>	<b>11</b>
3.1	Regimes of the cumulative distribution function . . . . .	11
3.2	Uncertainty analysis . . . . .	11
3.3	Spatiotemporal variability as a function of scale . . . . .	12
3.4	Estimation of the radial distribution function . . . . .	12

# 1 Deployment locations

The data presented in this paper were collected from 2 nearby locations in the deepwater central basin of UML. Their relative locations and deployment periods in 2012 are mapped in Fig. S1.

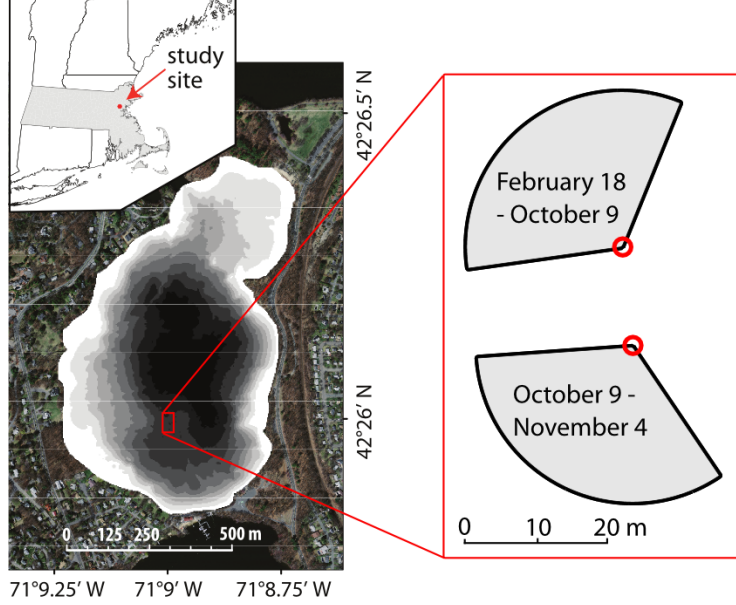


Figure S1: Map showing the relative locations and orientations of the 2 deployment locations where the data presented here were collected.

## 2 Flux estimation methods

### 2.1 Backscatter measurement using the Imagenex 837B

The Imagenex 837B Delta T multibeam profiling sonar does not measure backscatter cross-section directly, so we present here the method used to calibrate it for that purpose.

The pressure wave amplitude of the sound received by a sonar unit is that of the source, diminished by spherical spreading and attenuation, and increased by the magnitude of the target causing the reflection. The received amplitude  $P_{rec}$  after travel to and from targets with backscatter cross-section  $\sigma_{bs}$  at distance  $R$ , with spherical spreading, is:

$$\left(\frac{P_{rec}}{P_0}\right)^2 = \left(\frac{P_{src}(\theta)}{P_0}\right)^2 \left(\frac{R}{R_0}\right)^{-4} 10^{-\frac{2\alpha R}{10}} \frac{\sigma_{bs}}{R_0^2}, \quad (S1)$$

where  $P_{src}(\theta)$  is the directionally-dependent amplitude of the source signal,  $P_0$  and  $R_0$  are reference pressure and length values, and  $\alpha$  is a coefficient of acoustic attenuation in the water. The use of reference values facilitates handling the sonar equation in logarithmic form, though for the sake of clarity we will use SI units.

The Imagenex DeltaT reports an amplitude that is proportional to the received pressure in each pixel (beam for direction and sample for distance from the sonar head):

$$(a_{\Delta T})^2 = \left( k_a \frac{P_{rec}(\theta)}{P_0} \right)^2 G^2 \left( \frac{R}{R_0} \right)^2 10^{\frac{2\alpha R}{10}}, \quad (S2)$$

$$G = 10^{\frac{G_s}{20}} \left( \frac{G_d}{100} \right), \quad (S3)$$

where  $k_a$  is an unknown proportionality constant and  $G$  is the user-defined gain on the signal. The user-defined gain  $G$  depends on 2 parameters, the hardware “StartGain” ( $G_s$ ) and the software “DisplayGain” ( $G_d$ ) that scales the data into the 8-bit dynamic range. The power of 2 in  $R/R_0$  compensates for part of the geometric spreading and is applied as a time-varying gain (TVG) to the incoming signal. It is appropriate for quantifying the reflectivity of surface targets that extend past the incident area of the sonar pulse (which is proportional to  $R^2$ ), as is the case for the sediment surface in a bathymetric survey. Since  $k_a$  is Imagenex proprietary information, we define  $a_{rec} = k_a P_{rec}/P_0$  and  $a_{src}(\theta) = k_a P_{src}(\theta)/P_0$ . This way, Equations (S1) and (S2) can each be solved for  $a_{rec}$ :

$$a_{rec}^2 = a_{src}^2 \left( \frac{R}{R_0} \right)^{-4} 10^{\frac{-2\alpha R}{10}} \frac{\sigma_{bs}}{R_0^2} \quad (S4)$$

$$= \left( \frac{a_{\Delta T}}{G} \right)^2 \left( \frac{R}{R_0} \right)^{-2} 10^{\frac{-2\alpha R}{10}}. \quad (S5)$$

Setting these two equal and solving for  $\sigma_{bs}$  yields:

$$\sigma_{bs} = \left( \frac{a_{\Delta T} R}{a_{src}(\theta) G} \right)^2. \quad (S6)$$

For the data reported here,  $G_s = 20$  dB and  $G_d = 3$  so that  $G = 0.3$ . The source amplitude  $a_{src}(\theta)$  has two components: a base magnitude  $a_0$  and directional dependence, or horizontal beam pattern,  $B_h(\theta)$ :

$$a_{src}(\theta) = a_0 B_h(\theta). \quad (S7)$$

The horizontal beam pattern was estimated in a two-step process described below. The base magnitude  $a_0$  was then estimated using a standard 38.1 mm diameter tungsten-carbide calibration sphere in situ ( $\sigma_{bs} = 1.19 \times 10^{-4} \text{ m}^2$  for  $f = 260$  kHz). The sphere was raised and lowered through the sonar fan in a variety of locations ( $\theta$  and  $R$ ) to get a record of the maximum  $a_{\Delta T}$ . Equations (S6) and (S7) were then combined to solve for  $a_0$ , yielding estimates of  $a_0 = (3.2 \pm 0.7) \times 10^5$  for the unit used in this study.

## 2.2 Backscatter vs. flux for a multibeam sonar

Sonar is an effective tool for detecting gas bubbles in water because the large contrast in acoustic impedance (product of density and speed of sound) causes pressure waves—when emitted at an appropriate frequency—to reflect strongly off the surface of the bubble.

However, estimating the volume within gas bubbles that are detected by sonar is challenging because the magnitude of the sonar signal (the backscatter cross-section,  $\sigma_{bs}$ ), is roughly proportional to the total cross-sectional area of bubbles facing the sonar, not their volume. If the distribution of bubble sizes varies little compared with the number of bubbles insonified, the backscatter becomes proportional to the total bubble volume, and therefore the flux [1]. This “inverse” method has been demonstrated at marine ebullition sites using downward-looking, single-beam and split-beam echosounders used during ship-based surveys [1–3]. Here we develop an inverse method for estimating gas fluxes using a fixed-location, horizontally-oriented, profiling multibeam sonar.

While multibeam sonars are typically used with the fan oriented vertically for bathymetric profiling, we used the fan in a horizontal orientation to detect bubbles as they rose through it (Fig. 1c in the main text). A profiling multibeam sonar projects a pulse that is roughly planar and fan-shaped, and the received signal is processed to measure  $\sigma_{bs}$  as a function of both the distance from the sonar head (range) and the direction. A bubble stream rising through the sonar fan contributes to  $\sigma_{bs}$  in a spatially-compact collection of connected pixels. Each pixel, in turn, may insonify multiple bubbles because the fan-shaped pulse has a slight vertical extent ( $2.2^\circ$  half-power).

The backscattering measured by the sonar may be expressed as an integral over the radius of bubbles and over the vertical dimension,  $z$ :

$$\sigma_{bs} = \int \int N(r, z) \sigma_{bs}(r) B_v^2(z) dr dz, \quad (\text{S8})$$

where  $N(r, z)$  is the number of bubbles per radial and vertical unit distance, and  $\sigma_{bs}(r)$  is the backscatter from a single bubble of radius  $r$ , which may be modeled assuming a spherical bubble [4].  $B_v$  is the vertical beam pattern that reflects the sensitivity of the multibeam sonar in the alongship direction.

While the vertical position of individual bubbles within the sonar fan cannot be detected by the sonar, the impact of the vertical beam pattern can be accounted for by averaging measurements over a timescale equivalent to the rise time through the sonar fan (0.2–4 s). Over this timescale, the elevation dependence of  $N$  may be neglected, so that the integrals may be separated:

$$\bar{\sigma}_{bs} \approx \int B_v^2(z) dz \int N(r) \sigma_{bs}(r) dr \quad (\text{S9})$$

Because the profiling sonar has a relatively tight beam pattern (small  $\phi$ ), the relationship  $z = R \tan(\phi)$  may be approximated as  $z \approx R\phi$ . Applying this change of variables:

$$\bar{\sigma}_{bs} \approx R\phi_e \int N(r) \sigma_{bs}(r) dr, \quad (\text{S10})$$

$$\phi_e = \int B_v^2(\phi) d\phi, \quad (\text{S11})$$

where  $\phi_e$  is the equivalent beam angle: the angle equivalent to the vertical extent of the fan if the sensor had no sensitivity dropoff ( $B_v = 1$ ). The vertical beam pattern  $B_v^2(\phi)$  was

measured for the Imagenex 837B during calibration to be Gaussian with half-power angle  $\phi_0 = 2.2^\circ$  (Fig. S2):

$$B_v^2(\phi) \approx \exp \left[ -\ln(2) \left( \frac{\phi}{\phi_0/2} \right)^2 \right], \quad (\text{S12})$$

and, thus, the equivalent beam angle takes the form

$$\phi_e \approx \frac{\phi_0}{2} \sqrt{\frac{\pi}{\ln(2)}}. \quad (\text{S13})$$

where the second equation is the solution of Equations (S11) and (S12).

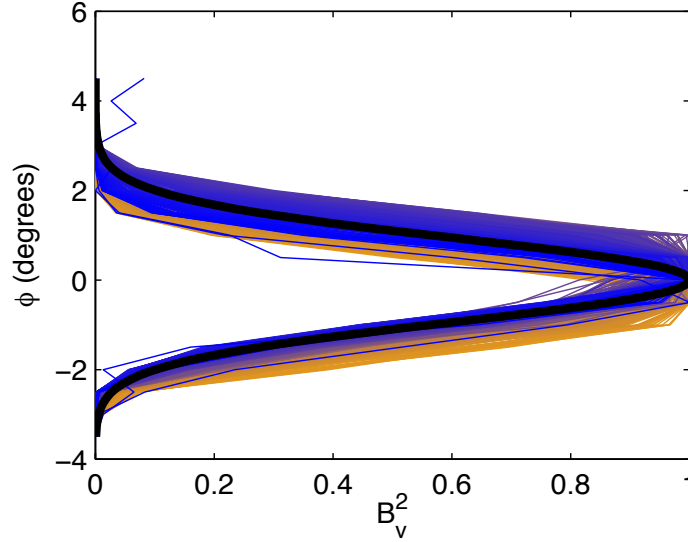


Figure S2: Vertical beam pattern,  $B_v(\phi)$ , for the Imagenex 837B, as measured in the ocean engineering tank at the UNH (colored lines), and with a Gaussian best-fit curve (black), with half-power angle  $\phi_0 = 2.2^\circ$  [Eq. (S12)]. Colors on lines indicate the horizontal (athwartship) beam measured, from  $-60^\circ$  (orange) to  $60^\circ$  (blue).

The volumetric gas flow rate through a pixel may similarly be expressed as an integral over the bubble radius:

$$Q = \int N(r)V(r)u_{rise}(r)dr, \quad (\text{S14})$$

where  $u_{rise}$  is the vertical rise velocity of the bubble, which may be modeled [5], and  $V(r) = (4/3)\pi r^3$  is the volume of an assumed-spherical bubble. By combining Equations (S10) and (S14), we obtain:

$$Q \approx \frac{\bar{\sigma}_{bs}}{R\phi_e} \frac{\int N(r)V(r)u_{rise}(r)dr}{\int N(r)\sigma_{bs}(r)dr}. \quad (\text{S15})$$

When the bubble size distribution (BSD),  $f(r)$ , is relatively constant, the number of bubbles may be expressed as the product of the overall bubble density  $N_0$  and the BSD,  $N(r) = N_0 f(r)$ . Applying this approximation allows  $N_0$  to cancel from the numerator and denominator, and a combined expression for the flow rate is:

$$Q \approx K \left( \frac{\bar{\sigma}_{bs}}{R} \right), \quad (\text{S16})$$

$$K = \frac{\int f(r) V(r) u_{rise}(r) dr}{\phi_e \int f(r) \sigma_{bs}(r) dr}. \quad (\text{S17})$$

The flow rate estimated by Eq. (S16) is subject to temporal smoothing because  $\bar{\sigma}_{bs}$  is measured over a timescale at least equivalent to the time a bubble takes to traverse the sonar fan. This smoothing does not impact estimates of the total volume because the smoothed flow rate is integrated over time. This equation permits theoretical calculation of the coefficient  $K$  for an arbitrary BSD. This may be compared with the coefficients used for the inverse method in single-beam and split-beam sonar units [1; 3].

Due to the high spatial resolution of the sonar, bubble streams typically activate a cluster of 2-20 connected pixels, depending on the flow rate and distance from the sonar head. Of interest for our analysis is the total flow rate from a bubble stream, so Eq. (S16) was applied to the sum of connected pixels that were active above a threshold of minimum flow rate:

$$Q_{tot} \approx K' \sum \left( \frac{\bar{\sigma}_{bs}}{R} \right), \quad (\text{S18})$$

$$K' = \frac{K}{f_{overlap}}, \quad (\text{S19})$$

where  $f_{overlap}$  is the degree of overlap between neighboring pixels and is measured empirically. As an alternative, one could analyze the maximum backscatter value from within the cluster of pixels, but such a measurement would be more sensitive to the horizontal beam pattern within each beam (Fig. S5) and would neglect the contribution of bubble streams active simultaneously and within a few pixel widths.

### Fixed bubble size distribution assumption

The approximation of a constant bubble size distribution (BSD) is most appropriate when the bubble plume is dense enough that the variations in the backscatter derive primarily from changes in the density of bubbles rather than their size. The ebullition events in UML are typically sparse, with only 1-20 bubbles per event, so that variations in the instantaneous backscatter may be primarily due to changes in bubble size and vertical position of the bubbles within the sonar fan. However, the use of 5-second temporal averaging to estimate the flow rate both accounts for the impact of the vertical beam pattern and increases the number of bubbles sampled for a given measurement, making the approximation of constant BSD more appropriate.

Some single-beam and split-beam sonar units independently report both the backscatter cross-section and the distribution of backscattering values from individual bubbles [5; 6] that allow simultaneous estimation of the BSD and flow rate. However, such detail is typically not available from multibeam sonar units like the one used in our study.

## Multiple scatter reflections

When multiple nearby bubbles are insonified, the received sonar signal amplitude may be composed of not only the direct backscatter from each of the bubbles, but also the multiple-scatter signal that bounces between multiple bubbles. The relative intensity of a multi-scatter signal depends on the scattering from each target and the distance between them. To estimate the importance of this effect, consider two identical bubbles separated from each other by distance  $D$  and from the sonar head by range  $R$ . The scattering from a gas bubble may be up to 10 times that of the backscattering for  $kr < 10$  [7], so the scattering cross-section from the multi-scatter signal ( $\sigma_{multi}$ ) is:

$$\sigma_{multi} \leq \frac{10\sigma_{bs}^2}{4\pi D^2}, \quad (S20)$$

$$\bar{\sigma}_{ms} = \frac{\sigma_{multi}}{\sigma_{bs}} \leq \frac{10\gamma}{4} \left(\frac{r}{D}\right)^2, \quad (S21)$$

where  $\gamma$  is the scattering normalized by the cross-sectional area. For bubbles in the size range of  $a \in [0.5, 5]$  mm,  $\gamma \approx 0.1$  [7] so that for inter-bubble distance  $D > 5$  mm,  $\bar{\sigma}_{ms} \leq 10^{-2}$ . If  $Q = Vu/D$ , where  $V$  is the bubble volume for bubbles rising in a homogeneous vertical stream, then we can define  $\bar{\sigma}_{ms}$  as a function of  $Q$  and  $r$ :

$$D = \frac{Vu}{Q} = \frac{4\pi r^3}{3Q}, \quad (S22)$$

$$\bar{\sigma}_{ms} \leq \frac{5\gamma}{2} \left(\frac{3Q}{4\pi ur^2}\right)^2. \quad (S23)$$

This allows us to define iso-lines of  $\bar{\sigma}_{ms}$  in the space of  $Q$  and  $r$ , a lower bound for  $Q$  required to make multi-scatter signals detectible at a given tolerance  $\bar{\sigma}_{ms}$ ,

$$Q \geq \sqrt{\frac{2\pi\bar{\sigma}_{ms}}{5\gamma}} \frac{4\pi ur^2}{3}. \quad (S24)$$

Thus, the flow rate threshold at a given tolerance for multi-scatter signals increases with the square of the bubble radius, and high-flow bubble streams with small bubbles are the most conducive to multi-scatter (Fig. S3). For the range of bubble sizes and flow rates observed in the lake, multi-scatter signals are expected to contribute typically less than 1% of the total sonar signal and only rarely up to 10%, so their influence is neglected.

## 2.3 Calibration experiment

This flux-estimation model was tested during a calibration experiment in the Ocean Engineering Tank at the University of New Hampshire (UNH). Gas was released at constant flow rates from an aperture that produced a fairly narrow range of bubble sizes, which were measured with underwater photographs. The rate of bubble release was measured using a passive hydrophone near the bubble outlet. The time-averaged sonar signal  $\bar{\sigma}_{bs}/R$  was summed over all the pixels activated by a given bubble stream, which typically ranged from 2–20 pixels depending on width of the plume and its distance  $R$  from the sonar head. This

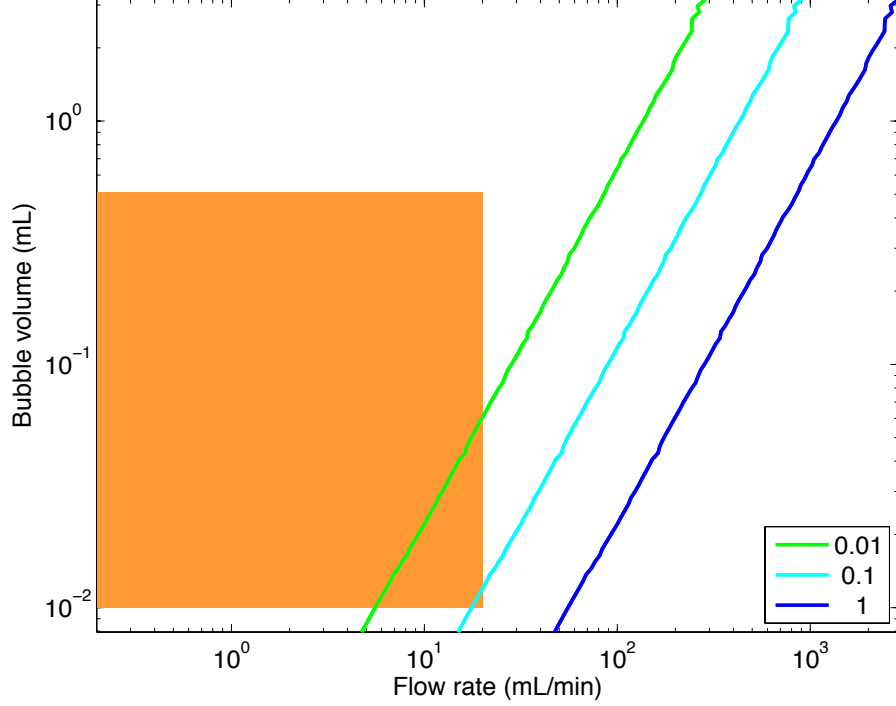


Figure S3: Normalized multiple-scatter reflection magnitude  $\bar{\sigma}_{ms}$  (isolines in legend) as a function of flow rate and bubble volume. The shaded orange region shows the range of bubble sizes and flow rates expected to be encountered, from the BSD [8] and from the limits on mean flow rate for distinguishing bubbles from anchor lines. In most cases we expect multi-scatter reflections to contribute less than 1% of the signal, and only above 10% for the cases of highest flow rates with smallest bubbles.

summed sonar signal was plotted against the flow rate for a range of  $Q$  (Fig. 1d in the main text). These measurements were compared against the modeled response for 3 different bubble size classes ranging from 1.1–2.5 mm in radius. The modeled response fit the data when  $f_{overlap} = 1.4$ .

### Bubble image analysis

In addition to passive acoustic methods, bubble photographs were used to estimate the bubble sizes. The observation area was back lit with a powerful underwater light behind a 1/4-inch translucent plastic diffuser panel. Individual images were taken every second for at least 1 minute during the calibration tests, and the bubbles were identified and sized automatically using MATLAB. Bubbles were identified by a best-fit ellipse on a group of nearby pixels that correspond to edges in intensity in the red channel. Edge pixels were identified using the Canny method, which identifies pixels in a gradient with magnitude above a given threshold. We used lower and upper thresholds of 0.0002 and 0.005, respectively, and a Gaussian filter with width of 1 pixel. Edge pixels were grouped with their neighbors using the density-based scan algorithm [9]. For these pixel groups, best-fit ellipses were identified using MATLAB’s `regionprops` function, and the radii were shrunk by 20% to match the



images [10] (Fig. 2.3). Bubble volumes were estimated assuming that the bubbles were oblate spheroids so that  $V = \frac{4}{3}\pi r_{\max}^2 r_{\min}$ , where  $r_{\max}$  and  $r_{\min}$  are the respective major and minor axes of an ellipse. Bubbles smaller than 0.5 mm in radius were rejected from the automated processing algorithm, to avoid spuriously treating image noise as bubbles.

Radii shrunk by 20 percent

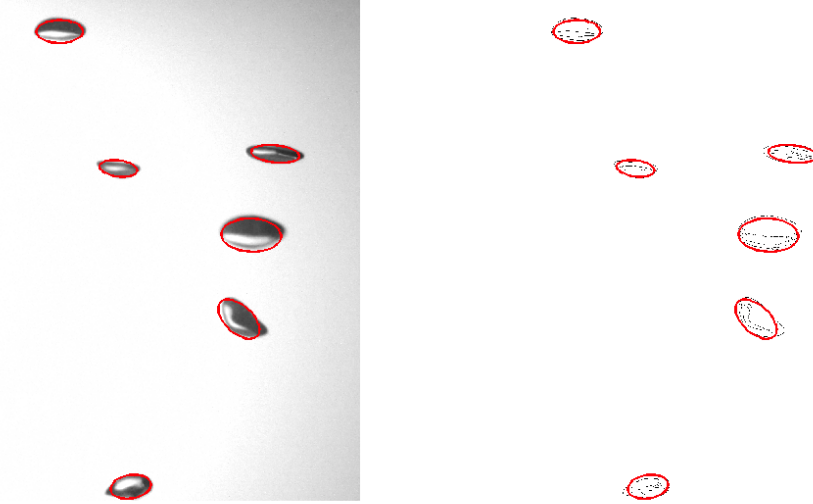


Figure S4: Automatic bubble identification from calibration images. Left: grayscale image with identified ellipses superimposed in red. Right: edge pixels with the same ellipses. In both cases, the radii are reduced by 20% from those identified using MATLAB’s `regionprops` tool.

## 2.4 Classification of events

Events were identified from the sonar data in a way appropriate for detecting and quantifying ebullition, although other targets can manifest themselves as bubble events. The bottom of UML is a fairly quiescent zone, with slow seich-driven current on the order of 5 cm/s and oxygen levels too low to support aerobic biota like fish. However, strong sonar returns were caused by ropes and chains connecting buoys to anchors. These targets can be clearly distinguished from bubbles by their persistence and slow lateral drift, which can be observed directly in animations of the sonar signal. We implemented an automated workflow, which classified the events using thresholds on their duration, total volume released, and intensity (mean and maximum flow rate). The values of these thresholds were chosen to as to achieve high rates of correct identification of both bubbles and anchors.

## 2.5 Beam pattern

Every sonar unit exhibits directionality dependence in the strength of the sonar returns. To correct for this dependence, we normalized the data with a beam pattern found through a combination of detailed calibration and tuning to eliminate the remaining large-scale pattern.

The beam pattern of an Imagenex 837B sonar unit was measured in the ocean engineering tank at UNH using a 38.1 mm diameter tungsten-carbide calibration sphere, using a rotating pole to turn the sonar head horizontally (athwartship) and a motorized spool and sensor to raise and lower the sphere vertically (alongship). Tests were carried out at 4 and 8 m, though the 8 m test was less reliable due to interactions with the wall in one direction. The high-resolution 4-m test shows a roughly Gaussian shape with a central peak and high-frequency oscillations that correspond to the sensitivity within each beam (Fig. S5).

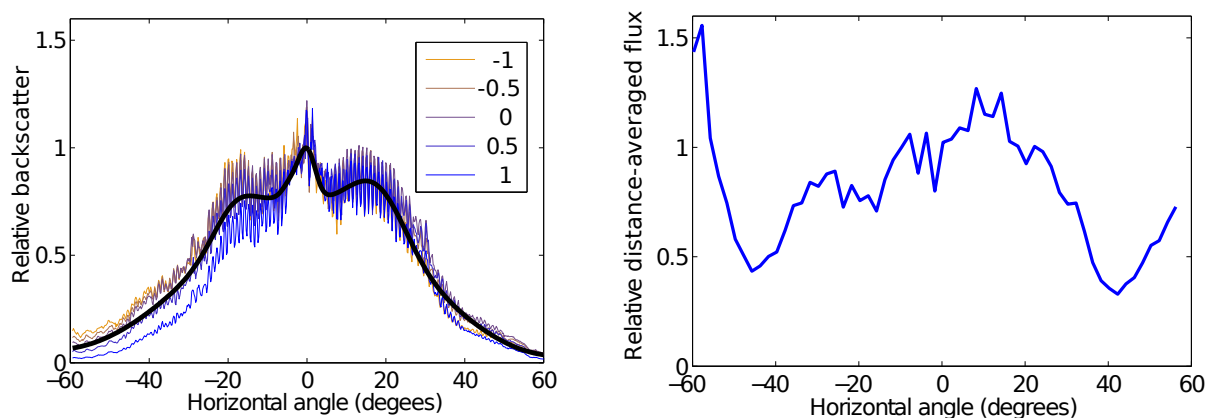


Figure S5: Left: beam pattern from a calibration sphere shows a roughly Gaussian shape. The variability in backscatter across each 1-degree beam corresponds to the sensitivity within each beam. Each line represents the pattern at a different elevation angle (legend in degrees). The black line superimposed is the calibration-sphere beam pattern. Right: average flux values as a function of direction ( $2^\circ$  resolution) from the April 2012 data corrected with the uncorrected beam pattern, normalized to the value in the central beams.

When corrected with the calibration-sphere beam pattern intensity, the resulting long-term ebullitive flux data still showed a recognizable residual directional dependence (Fig. S5, right). The symmetry and temporal consistency of the residual directional dependence indicates that it more likely arises from the measurement system than from an actual spatial pattern of ebullition heterogeneity. This suggests that the beam pattern measured with the calibration sphere did not fully account for the field measurements at UML. This discrepancy may be due to the nearby walls in the tank impacting the measured signal, although the beam pattern measurements were carried out at a closer range than any wall reflections. The discrepancy may also arise from differences between the immobile sphere used for calibration and rising bubble targets detected in the lake. Motion of the bubbles may decorrelate the sonar pulse in time, spreading the sonar signal over neighboring beams and reducing the magnitude of the flow rate estimate. This effect is expected to play a larger role in the outer beams. Ultimately, to address this issue, the residual directional dependence of the flux record was used to correct the beam pattern.

### 3 Analysis of flux magnitudes

#### 3.1 Regimes of the cumulative distribution function

Approximately 98% of the flux measurements follow a lognormal trend over intermediate magnitudes (0.1-100 mg/m<sup>2</sup>/day), with parameters log-mean  $\mu = 0.62$  and log-standard deviation  $\sigma = 1.8$  (Fig. 2c in the main text). Smaller and larger flux measurements are fit by lognormal models with smaller variance,  $\sigma = 0.5$  and 1.0, respectively. A flux distribution composed of multiple lognormal regimes was also observed at natural hydrocarbon seeps in a marine setting, although in that study the high-flux regime constituted 13% of the flux measurements, compared with  $\sim 1\%$  here [11].

#### 3.2 Uncertainty analysis

The uncertainty associated with flux measurements is estimated to be  $\sim 70\%$  and is primarily derived from variability and uncertainty in the bubble size distribution (BSD), although the uncertainty in bubble rise speed, source amplitude, beam pattern and instrument noise were considered. The flux may be expressed as:

$$q = cK \sum_{i=1}^{n_{event}} \sum_{j=1}^{n_{ping}} \left( \frac{\bar{\sigma}_{bs}}{R} \right) \quad (S25)$$

$$= \frac{cK}{a_0} \sum_{i=1}^{n_{event}} \sum_{j=1}^{n_{ping}} \left( \frac{a_{\Delta TR}}{B_h(\theta)G} \right), \quad (S26)$$

$$c = \frac{\Delta t_{ping}}{\Delta t_{sample} A}, \quad (S27)$$

where  $K$  is the calibration coefficient (L/day/m),  $\Delta t_{ping}$  is the time between pings,  $n_{ping}$  is the number of pings in a given event, and  $\Delta t_{sample}$  and  $A$  are the duration and observation area of the sample over which the flux is calculated from the sum of  $n_{event}$  events. The backscattering is calculated using the instrument-reported sonar amplitude,  $a_{\Delta T}$ , and the source level amplitude  $a_0$ .

The product  $n_{ping} \times n_{event}$  is large for most flux estimates presented in this work, and the averaging over so many measurements makes the contribution from instrument noise negligible. However, the parameters  $K$ ,  $a_0$  and  $B_h(\theta)$  all have significant uncertainty. Each is independent and contributes multiplicatively to  $q$ , so the relative uncertainty in  $q$  can be estimated using propagation of uncertainty:

$$\frac{\text{var}(q)}{q^2} \approx \frac{\text{var}(K)}{K^2} + \frac{\text{var}(a_0)}{a_0^2} + \frac{\text{var}(B_h)}{B_h^2}. \quad (S28)$$

The uncertainty associated with the calibration coefficient  $K$  derives from 3 sources: uncertainty in the bubble rise speed  $u_{rise}$ , uncertainty in the long-term BSD, and short-term variations in the BSD (Eq. (S17)).

A number of models for bubble rise speed have been developed, and the nature of the bubble interface (“clean” vs. “dirty”) can cause discrepancies of up to  $\approx 40\%$ . However, in

a study of marine gas fluxes using the same inverse hydroacoustic method, the relative error between 7 different models contributed only 15% relative uncertainty in  $K$  and  $Q$  [3]. Plumes of rising bubbles may create upwelling velocities that allow bubbles to rise faster than the terminal velocity of an individual bubble. However, for the relatively low flow rates observed in UML ( $Q \leq 20$  mL/min), upwelling velocities are observed to be limited to 2 cm/s, less than 10% of the terminal velocity [12]. Thus, we estimate a combined relative uncertainty of 18% for the rise velocity.

The uncertainty in the long-term BSD may be estimated as  $\approx 23\%$  using the relative difference in calibration coefficients calculated using BSDs from UML [8] and Lake Kinneret [5]. The final source of uncertainty in  $K$  is from short-term variations in the BSD, over timescales larger than the 5-second averaging period used to measure  $\bar{\sigma}_{bs}$ . We estimate that BSD varies from the long-term mean by up to  $\sim 50\%$  in the radius. If these factors have a multiplicative effect, then the combined relative uncertainty is  $\sqrt{\text{var}(K)}/K \approx 58\%$ .

The relative uncertainty in  $a_0$  is estimated to be  $\approx 22\%$  from the variability in values measured across the sonar fan in UML. The relative uncertainty in  $B_h(\theta)$  is estimated to be  $\approx 36\%$ , from the coefficient of variance in the flux-derived correction to the beam pattern (Fig. S5, right) across  $\theta$ . Using these values in Eq. (S28), we find a combined relative uncertainty of  $\sqrt{\text{var}(q)}/q \approx 70\%$ . Over long time periods, the large number of bubbles samples will converge towards the system-wide BSD and reduce the uncertainty in  $K$ , the primary contributor to the overall uncertainty. However, because of the inverse relationship between  $K$  and  $r$ , this convergence in BSD does not guarantee that the flux estimates will converge on the long-term average if there is significant variability in the apparent BSD.

### 3.3 Spatiotemporal variability as a function of scale

The flux estimates from the deployment from February 18–June 1, 2012 were subsampled uniformly in space and time (gridded in space and time) at different spatial and temporal scales, and the fraction of subsamples that fell within  $\pm 50\%$  of the long-term, global mean flux of 7 mg/m<sup>2</sup>/day are shown in Fig. S6. The fraction of samples in the interval generally increases with larger spatial and temporal scales, reflecting the rate at which larger-scale, longer-duration observations become more likely to represent the overall mean. Some slight non-monotonicity in the trend may be attributed to time periods where the sensor was inactive. The long-duration (40 day) samples converge to 1 in the limit as the spatial scale increases to 8 m, but for finer spatial resolution significant heterogeneity remains. Similarly, the 8-m samples still show significant temporal variability for samples shorter than 10 days.

### 3.4 Estimation of the radial distribution function

To account for the enhanced importance of events releasing large volumes of gas, the volume-weighted RDF was estimated using the marked pair correlation function [15, Eqn. (5.3.54)] and the mark-sum intensity [15, Eqns. (4.2.20) and (5.2.2)], with the volume of gas released during an event serving as its mark. The isotropized set covariance was estimated numerically for the irregular observation window and used in place of the pair-specific displacement area [16, Eqn. (9.29)]. The method was confirmed as unbiased using simulations of a CSR process on the same domain used by the sonar.

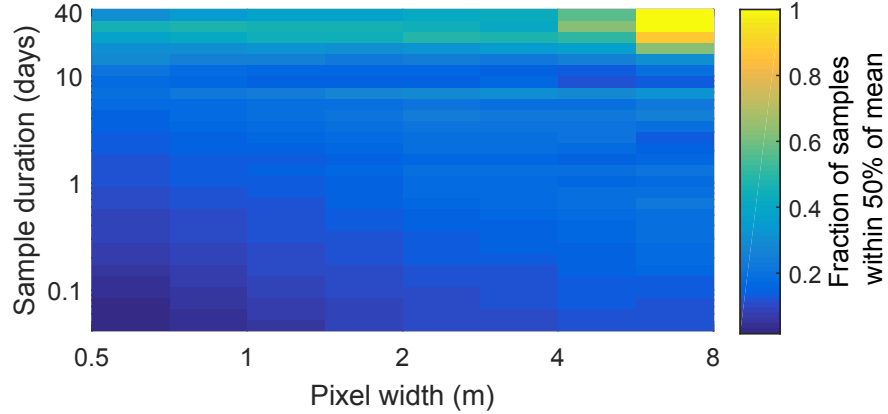


Figure S6: Spatiotemporal variability as a function of scale of measurement. Color scale represent the fraction of subsamples of the data from February 18–June 1, 2012 that fall within  $\pm 50\%$  of the long-term, global average flux value, as a function of the spatial extent for gridding of fluxes (0.5–8 m) and duration (1 hr–40 days). Samples shorter than 1 day in duration or with a spatial scale on the order of 1 m (as with most bubble traps) are less than 50% likely to measure a sample within  $\pm 50\%$  of the long-term mean. Only multi-week samples with spatial scale over 5 m always fell within  $\pm 50\%$ .

Data from Feb 18–May 31, 2012 were divided into segments of 20 min in duration, which were classified as high- or low-flux relative to the average over the whole deployment period. From these segments, continuous samples of durations from 10 min to 4 days were analyzed to test the impact of observation time on the spatial signature observed.

The sonar technique provides sufficient resolution to confirm that the outlets are distinct, as the maximum pixel separation of 0.35 m is finer than the event separation of  $\geq 0.5$  m, and bubbles are unlikely to drift laterally by more than 0.1 m during their rise of  $\sim 1.5$  m from the sediment surface to the sonar fan, given typical lateral currents on the scale of 1 cm/s (observed from slow, spatially-coherent drift of low-intensity signals reflecting suspended flocs) and bubble rise velocities of 20 – 25 cm/s [5]. It is possible that non-bubble targets, such as anchor lines, contaminate the RDF sufficiently to create an appearance of spatial clustering in the mean, but these constitute  $\leq 6\%$  of the flux so should not create the pronounced effect seen here (Figs. 3d,e in the main text).

## Acknowledgments

We thank Emile Bergeron and Dann Blackwood of the USGS Woods Hole operations staff, Coach Kenneth Legler and the Tufts Sailing Team, the Winchester Boat Club, Doug Wilson and the Imagenex Technology Corporation, Jens Greinert of GEOMAR, and Kyle Delwiche and Hannah Wood of MIT. This work was supported by the U.S. National Science Foundation (Award No. 1045193) and the U.S. Department of Energy (Grant No. DE-FE0013999). Any use of a trade, product, or firm name is for descriptive purposes only and does not imply endorsement by the U.S. Government.

## Supplemental References

- S1. Muyakshin, S. I. & Sauter, E. The hydroacoustic method for the quantification of the gas flux from a submersed bubble plume. *Oceanology* **50**, 1045–1051 (2010).
- S2. Weber, T. C. *et al.* Acoustic estimates of methane gas flux from the seabed in a 6000 km<sup>2</sup> region in the northern Gulf of Mexico. *Geochemistry, Geophysics, Geosystems* **15**, 1911–1925 (2014).
- S3. Veloso, M., Greinert, J., Mienert, J. & De Batist, M. A new methodology for quantifying bubble flow rates in deep water using splitbeam echosounders: Examples from the Arctic offshore NW-Svalbard. *Limnology and Oceanography-Methods* **13**, 267–287 (2015).
- S4. Anderson, V. C. Sound scattering from a fluid sphere. *Journal of the Acoustical Society of America* **22**, 426–431 (1950).
- S5. Ostrovsky, I., McGinnis, D. F., Lapidus, L. & Eckert, W. Quantifying gas ebullition with echosounder: the role of methane transport by bubbles in a medium-sized lake. *Limnology and Oceanography-Methods* **6**, 105–118 (2008).
- S6. DelSontro, T., McGinnis, D. F., Wehrli, B. & Ostrovsky, I. Size does matter: Importance of large bubbles and small-scale hot spots for methane transport. *Environmental Science & Technology* **49**, 12681276 (2015).
- S7. Medwin, H. & Clay, S. *Fundamentals of Acoustical Oceanography (Applications of Modern Acoustics)* (Academic Press Limited, 1998).
- S8. Delwiche, K., Senft-Grupp, S. & Hemond, H. A novel optical sensor designed to measure methane bubble sizes in-situ. *Limnology and Oceanography - Methods* , doi:10.1002/lom3.10060 (2015).
- S9. Daszykowski, M., Walczak, B., & Massart, D.L. Density-based clustering for exploration of analytical data. *Analytical and Bioanalytical Chemistry* **380**, 370–372 (2004).
- S10. Thomanek, K., Zielinski, O., Sahling, H. & Bohrmann, G. Automated gas bubble imaging at sea floor – a new method of in situ gas flux quantification. *Ocean Science* **6**, 549–562 (2010).
- S11. Clark, J. F., Washburn, L. & Emery, K. S. Variability of gas composition and flux intensity in natural marine hydrocarbon seeps. *Geo-Marine Letters* **30**, 379–388 (2010).
- S12. Leifer, I. Characteristics and scaling of bubble plumes from marine hydrocarbon seepage in the Coal Oil Point seep field. *Journal of Geophysical Research* **115**, C11014 (2010).
- S13. Wik, M., Crill, P. M., Bastviken, D., Danielsson, A. & Norback, E. Bubbles trapped in arctic lake ice: Potential implications for methane emissions. *Journal of Geophysical Research* **116**, G03044 (2011).

- S14. Walter Anthony, K. M. & Anthony, P. Constraining spatial variability of methane ebullition seeps in thermokarst lakes using point process models. *Journal of Geophysical Research* **118**, 1015–1034 (2013).
- S15. Illian, J., Penttinen, A., Stoyan, H. & Stoyan, D. *Statistical Analysis and Modelling of Spatial Point Patterns* (Wiley, West Sussex, England, 2008).
- S16. Ohser, J. & Mcklich, F. *Statistical Analysis of Microstructures in Materials Science* (Wiley, West Sussex, England, 2000).